Next Materials 12 (2026) 102284

Contents lists available at ScienceDirect

Next Materials

journal homepage: www.sciencedirect.com/journal/next-materials

Research article

Mechanism behind enhanced electrical performance of doped nanostructured tin oxide - surface defect engineering vs dopant electron donation

Abubakar Sadiq Yusuf [a,b,c,1], Martin Markwitz [b,d,e,1], Zhan Chen [a], Maziar Ramezani [a], John V. Kennedy [b,e,*], Holger Fiedler [b]

[a] School of Engineering, Computer and Mathematical Sciences, Auckland University of Technology, PO Box 92006, Auckland 1142, New Zealand
[b] National Isotope Centre, Earth Sciences New Zealand, PO Box 30368, Lower Hutt, 5010 New Zealand
[c] School of Physical Sciences, Department of Physics, Federal University of Technology, PMB 65, Minna, Niger State, Nigeria
[d] School of Chemical and Physical Sciences, Victoria University of Wellington, PO Box 600, Wellington 6140, New Zealand
[e] The MacDiarmid Institute for Advanced Materials and Nanotechnology, Victoria University of Wellington, PO Box 600, Wellington 6140, New Zealand

ARTICLE INFO

Keywords:
Tin oxide
Antimony
Xenon
Implantation
Annealing
Resistivity

ABSTRACT

Tin dioxide (SnO_2), with its high optical transmittance and inherent n-type conductivity, is a promising electron transport layer (ETL) material. For application as an ETL material, it is desirable to enhance the charge carrier concentration and mobility of SnO_2 to maximise its electron conductivity. This is typically achieved by incorporation of dopants which donate electrons into the material. Here we demonstrate that the generation of defects within SnO_2 controls the electrical properties of the doped material. The effects of solely defect engineering are demonstrated by ion implantation of the noble gas Xenon (Xe) into SnO_2. Xe was chosen since it is similar in mass to the well-known chemical dopant antimony (Sb), which simplifies matching of the implantation conditions to cause the same number of ion-induced defects and implanted element distribution, for straightforward comparisons. Our results show that there is no effect of electron donation of Sb, since the resistivities of the film after Xe and Sb implantations are identical. After annealing at 200° C, both implanted films show comparable resistivities of (160.8 ± 4.7) μΩ cm and (150.2 ± 8.7) μΩ cm for Sb and Xe, respectively. Differences only emerge at higher annealing temperatures due to the improved stability of defects after Sb doping. Sb doping increases conductivity through defects alone, with no electron donation effects. This will allow for development of better doping strategies to optimise defect engineering and increase performance of SnO_2:Sb for ETL materials.

1. Introduction

ETLs are indispensable in perovskite solar cell (PSC) technology, where they facilitate efficient electron extraction, transport, and collection from the photoactive perovskite layer to the electrode [1,2]. Elevated ETL conductivity reduces series resistance, enhancing charge transfer and minimizing energy losses, which are critical for improving power conversion efficiency (PCE) [3]. Tin dioxide has emerged as a semiconductor material used in diverse applications, such as solar energy conversion, catalysis, and gas sensing [4,5], and it is especially well-suited as a transparent electrode in thin-film optoelectronic devices [6]. Being a wide-bandgap semiconductor (>3.6 eV), is highly regarded as an ETL material due to it's inherent n-type conductivity, and low formation energy of donor defects such as oxygen vacancies (V_O) and tin interstitials (Sn_i) [7]. Intrinsic SnO_2 films exhibit moderate conductivity ($10–10^2$ S/cm) which limits their potential for high-performance PSCs [8,9]. Efforts to enhance electrical conductivity often involve extrinsic doping with pentavalent cations, with Sb being particularly effective [10,11]. Optimal Sb doping 2 wt% has been shown to yield excellent optical transparency (>85%), low sheet resistance (32 Ω $\square^{-1}$), high carrier concentration (6.35×10^{20} cm^{-3}), and high mobility 32 cm^2 V^{-1} s^{-1} [12]. Additionally, thermal annealing treatments are commonly used to further improve optical and electrical characteristics [13,14]. Numerous investigations have shown that SnO_2 and SnO_2:Sb layers

* Corresponding author at: National Isotope Centre, Earth Sciences New Zealand, PO Box 30368, Lower Hutt 5010, New Zealand.
E-mail address: john.kennedy@earthsciences.nz (J.V. Kennedy).
[1] Present address: Robinson Research Institute, Victoria University of Wellington, PO Box 33436, Petone 5046, New Zealand

https://doi.org/10.1016/j.nxmate.2026.102284
Received 2 May 2025; Received in revised form 23 March 2026; Accepted 13 May 2026
Available online 21 May 2026

exhibit superior thermal stability compared to comparable transparent electrodes made of ZnO or In_2O_3 compounds [15,16]. While promising, the effects of Sb doping and annealing remain highly dependent on the initial properties of the SnO_2 films and the fabrication process [17]. However, Bai and colleagues reported that low-temperature solution-processed Sb-doped SnO_2 films have demonstrated significant enhancements in conductivity, fill factor (FF), and efficiency in PSCs, compared to uniform thin films [18]. Hence, the combined effects of thermal annealing, dopant activation, and lattice disorder to optimise conductivity and transparency of SnO_2 films require deeper investigation, especially on non-uniform thin films.

Ion implantation is a versatile technique for tailoring the properties of transparent wide-bandgap semiconductors for diverse optoelectronic applications [19]. Noble gas dopants can provide insights into radiation-induced disorder, while electrically active dopants, such as Sb, can also enhance conductivity by introducing free carriers [20]. Post-implantation annealing not only activates dopants but also repairs radiation-induced disorder. Therefore, using ion implantation and annealing, it can be determined whether property changes after doping are due to lattice damage, introduction of free carriers, or both. However, the interplay between dopant-induced chemical effects and ion radiation damage in SnO_2 remains poorly understood.

Further, previous studies of ion beam implanted Sb into SnO_2 were based on uniform thin films [17], leaving a gap in understanding of the behavior of doped colloidal SnO_2 films. We have previously demonstrated that the implantation of the noble gas Ar, has a significant effect on transparency and electrical conductivity, with an overall decrease of conductivity in Ar-doped SnO_2 after annealing at 200℃ [21]. However, none of the previous studies could separate the effect of chemical doping and the introduced disorder into SnO_2.

Hence there are conflicting information on which mechanism dominates charge transport in SnO_2. One option is the formation of oxygen vacancies to solely dominate the resistivity [7,20,22]. In contrast, chemical doping by Sb through an electron donation has been postulated to increase conductivity [12,23,24]. This knowledge can be advanced by conducting a comparative study in which Sb and noble gas Xe ions are implanted into colloidal SnO_2 thin films with identical acceleration energy and to the same fluence. The similar mass of Sb and Xe implies that the collision cascade between both elements are comparable, leading to an almost identical formation of oxygen vacancies. Hence, any difference in conductivity after Xe and Sb can be attributed to the chemical difference and electron donation of Sb. This is an established approach to distinguish if an underlying change of material parameters originates from chemical effects (electron donation) or vacancy generation (defect engineering) [25].

2. Experimental methods

The substrates were ultrasonically cleaned in acetone followed by ethanol and then deionized water for 10 min each. Before the coating of the SnO_2, a UV/Ozone treatment was employed on the substrates for 30 min. The 15 wt% tin (IV) oxide SnO_2 aqueous colloidal dispersion in H_2O was purchased from Alfa Aesar. We observed that the colloidal SnO_2 films contained Zr impurities. Tin oxide thin films were coated onto microscope glass and Si(001) substrates measuring 10 × 10 mm^2. The solutions were spin-coated by using a spin coater (L2001A-0920, Ossila) with a one-step process at 2000 rpm for 30 s. The spin-coated samples were dried at 100 °C for 5 min and subsequently annealed under air atmosphere conditions at 150 °C for 1 h. The resulting colloidal film had a thickness of 90 nm.

Sb and Xe ion implantation in as-prepared SnO_2 colloidal thin film was performed at the GNS Science low-energy ion implanter [26] using acceleration energies of 55 keV, resulting in a projected range (R_P) of 34 nm. The energy for the implantation depth was determined using TRIM-Dynamic (T-DYN), a Monte-Carlo ion implantation algorithm that utilizes the binary collision approximation. The T-DYN calculated implantation depth profiles are shown in Figure S1 [27]. The fluences utilized in this study were 5 × 10^{14} ions/cm^2, 1 × 10^{15} ions/cm^2, 3 × 10^{15} ions/cm^2, and 5 × 10^{15} ions/cm^2, resulting in peak Sb and Xe concentrations at the projected range of 0.3%, 0.6%, 1.8%, and 2.9%, respectively. All samples were implanted with ion beam current densities below 1 μA cm^{-2}.

X-ray photoelectron spectroscopy (XPS) analysis was performed to investigate the chemical composition using an ESCALAB250Xi instrument equipped with a monochromated Al K α_1 X-ray source with an energy of (1486.68 eV). The samples were *in situ* etched for 60 s with Ar^+. The data analysis was conducted using CasaXPS [28]. The binding energy was calibrated to the known SnO_2 486.7 eV binding energy of the Sn $3d_{5/2}$ peak with an uncertainty of 0.2 eV [29]. The structural properties were evaluated with x-ray diffraction (XRD) using a Rigaku SmartLab x-ray diffractometer with a Cu X-ray source (Cu K α_1 λ = 1.540 Å, Cu K α_2 λ = 1.544 Å) with a grazing incidence angle of $\omega = 1.5°$. The film thickness was measured using Rutherford backscattering spectrometry (RBS) with the backscattering detector located at 165° relative to the incident 2.0 MeV $^4He^+$ beam to a charge of 20 μC [30]. To provide ohmic contacts for electrical measurements, the corners of the SnO_2 colloidal films were coated with silver paste. These contacts were used for conducting four contacts van der Pauw electrical, and Hall effect measurements to determine the samples' electrical resistivity, Hall carrier concentration, and Hall carrier mobility. The measurements were performed using an Ecopia HMS-3000 Hall probe device with a 0.55 T magnet. Electrical characteristics at room temperature were tested four times for each sample orientation, from which the average value and standard deviations were obtained. The colloidal SnO_2 films visible transmittance to light was measured between 300 and 900 nm transmittance spectrum using a Perkin Elmer Lambda 365 spectrophotometer.

3. Results and discussion

The crystal structure and orientation of both the as-deposited and Sb^+-implanted SnO_2 colloidal films were examined using X-ray diffraction (XRD). Fig. 1a presents grazing incidence X-ray diffraction patterns for the as-deposited and antimony-implanted SnO_2 thin films. The XRD data confirm the preferred orientation of the SnO_2 films along the (110) plane, indicating a tetragonal rutile SnO_2 structure (JCPDS No. 01–090–6586). This orientation, thermodynamically preferred for thin film growth, is typical for spin coating processes due to the low surface energy of the (110) plane, promoting film stability as noted in the review by Batzill and Diebold on rutile-structured SnO_2 [31]. Fig. 1b shows that the intensity of the colloidal SnO_2(110) peak decreases after Sb^+ implantation at fluences of 5 × 10^{14}, 1 × 10^{15}, 3 × 10^{15}, and 5 × 10^{15} ions/cm^2. The as-deposited SnO_2 colloidal film has a lattice constant of 4.74 ± 0.01 Å, which remains unchanged even after implantation with the highest fluence of 5 × 10^{15} ions/cm^2. Similarly, the lattice constant c remains at 3.19 ± 0.01 Å, consistent with the accepted values for tetragonal rutile SnO_2 [31]. A similar effect was noted for the Xe^+-implanted samples, the XRD patterns of which are included in Figure S5.

XPS was employed to examine the surface composition of SnO_2 colloidal thin films implanted with antimony. Fig. 2 shows the XPS survey spectra (60 s Ar^+ etched) of an as-deposited and a 5 × 10^{15} ions/cm^2 implanted sample with fluence corresponding to 3 Sb.% for as-implanted and annealed SnO_2 colloidal films. The survey spectra identify the presence of tin, oxygen, carbon, and zirconium, in the as-deposited sample, and antimony in the 5 × 10^{15} ions/cm^2 implanted sample. The XPS measurements show that the as-deposited SnO_2 colloidal film has an atomic composition of 38.5% Sn, 59.4% O and 2.3% Zr, while the colloidal SnO_2 film implanted with a fluence of 5 × 10^{15} Sb cm^{-2} were 1.4% Sb, 35.2% Sn, 61.4% O and 2.1% Zr. The surface Sn:O ratio remained near 1:1.6 displaying a high concentration of oxygen vacancies near the film surface. RBS measurements of these

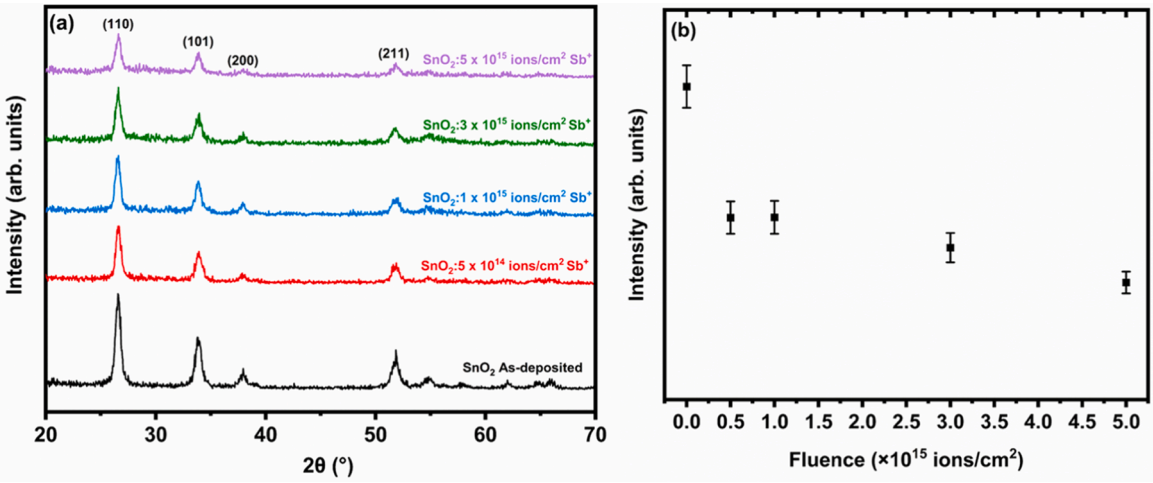

Fig. 1. (a) GIXRD patterns of the SnO_2 colloidal film after Sb^+ implantation. (b) SnO_2(110) peak intensity evolution as a function of fluence.

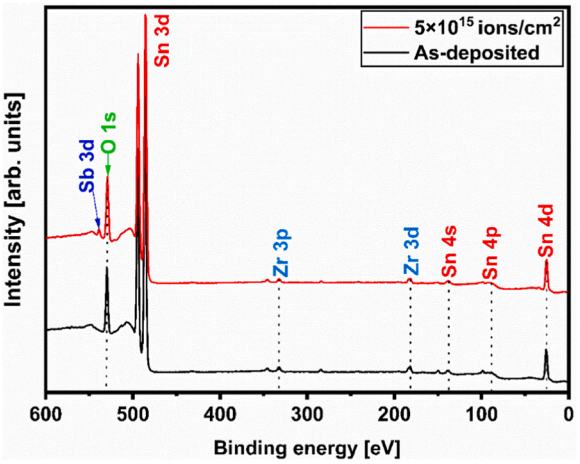

Fig. 2. XPS survey spectra of as-deposited and 5×10^{15} ions/cm^2 Sb^+ implanted SnO_2 colloidal thin films.

films (Figure S2) with the data analyzed with SIMNRA shows that the films have a bulk Sn:O ratio of 1:2 [32].

Fig. 3a shows that the implanted sample there is a notable increase in a low binding energy shoulder peak for the Sn 3d core level, suggesting an enhanced electron density through Sb doping. Fig. 3b shows that the binding energy values of the $3d_{5/2}$ core level of Zirconium (182.3 eV) associated with the Zr^{4+} oxide (ZrO_2) oxidation state were consistent with reported values from literature [33]. Similarly, to the Sn 3d core levels, the Zr 3p core level splits into a ZrO_x peak with reduced binding energy. The O 1 s and Sb 3d core levels are depicted in Fig. 2c which show the presence of a pair of oxygen peaks associated with lattice O^{2-} derived from tin oxides. The peak at 530.5 eV is attributed to O^{2-} anions bonding to Sn^{4+} cations in the stoichiometric SnO_2 lattice [34], while the peak at 530.8 eV corresponds to O^{2-} ions located in oxygen-deficient regions of SnO_2 [22]. Notably, in the implanted sample a low binding energy oxygen peak also appears, which is possibly related to the change in oxidation states of the Sn and Zr. In the same spectral region as the O 1 s core level, Sb $3d_{5/2}$ and Sb $3d_{3/2}$ peaks are found in the implanted sample. The Sb $3d_{3/2}$ peak is very broad, justifying a subdivision into two peaks, located at binding energies of 539.7 eV and 540.5 eV which correspond to Sb^{3+} and Sb^{5+}, respectively [35].

The UV–VIS transmittance spectra (Fig. 4) were acquired to determine the optical properties of the antimony and xenon implanted SnO_2 colloidal thin films deposited on soda-lime glass substrates. Optical transparency decreases as Sb^+ is incorporated into SnO_2 colloidal films in the wavelength range between 400 nm to 500 nm, while for longer wavelengths from 600 nm to 900 nm, the transparency of the implanted colloidal film increases (Fig. 4a). Generally, the transparency decreases with enhanced implantation fluence. Below 400 nm, the transmittance rapidly declines due to SnO_2 absorption. The UV-Vis data are consistent with implantation-induced disorder which may introduce more optical absorption centers [36]. Xenon was separately implanted into identically prepared and processed SnO_2 colloidal films, and no variation in lattice constant due to ion implantation were observed, consistent with previous results from argon implantation [21]. In addition, the UV–VIS results showed a consistent decrease in transparency (400 – 900 nm) with increasing implantation fluence (Fig. 4b).

Hall effect measurements were performed using the van der Pauw method at room temperature to determine the resistivity (ρ), Hall mobility (μ_H), and Hall carrier concentration (n_H) of the SnO_2 colloidal films. The electrical measurements are summarized in Tables S3 and S4, for the Sb and Xe-implanted samples, respectively. All films exhibited n-type conductivity, confirmed by the negative Hall coefficients. The n-type conductivity originates from shallow donor levels created by oxygen vacancies and interstitial tin ions in the SnO_2 lattice [37,38]. The carrier concentration was calculated from the Hall coefficient using the expression $n_H = qR_H^{-1}$, where the electron charge and Hall coefficients are q and R_H, respectively. The Hall carrier mobility was calculated from the Hall coefficient and resistivity with $\mu_H = R_H/\rho$. The Hall factor was assumed to be unitary due to the high carrier concentrations. For the as-deposited SnO_2 colloidal films, the resistivity, mobility, and carrier concentration were measured as (192.1 ± 5.5) μΩ cm, (41.5 ± 1.2) $cm^2 \cdot V^{-1} \cdot s^{-1}$, and (7.8 ± 0.2)× 10^{20} cm^{-3}, respectively. These values are consistent with ranges reported in the literature, despite different fabrication methods [39].

Fig. 5 presents a detailed analysis of electrical resistivity (ρ) data obtained from room temperature electrical measurements for the (a) Sb-implanted and (b) Xe-implanted samples. The as-deposited film exhibited an electrical resistivity (ρ) of (192.1 ± 5.5) μΩ cm. Following Sb ion implantation, notable changes in the measured electronic properties were observed. Films implanted with an Sb fluence of 3×10^{15} ions/cm^2 demonstrated an increase in resistivity to (316.1 ± 8.8) μΩ cm. Interestingly, at a higher fluence of 5×10^{15} ions/cm^2, a slight reduction in resistivity to (298.6 ± 8.6) μΩ cm was noted, although this value still represented a significant increase compared to the as-deposited film. Annealing at 200 °C in air led to a consistent decrease in resistivity. The samples with the highest fluence (5×10^{15} ions/cm^2) possessed the lowest resistivities of (160.8 ± 4.7) μΩ cm and (150.2 ± 8.7) μΩ cm for Sb and Xe implantations, respectively. However,

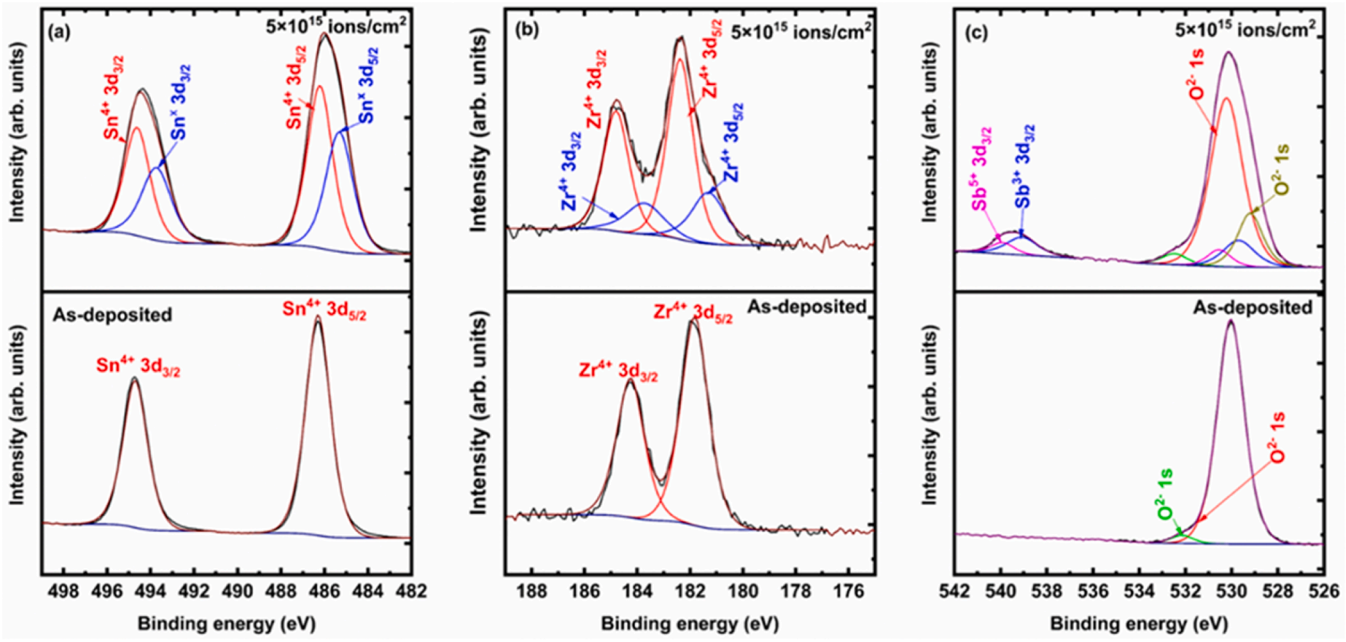

Fig. 3. High resolution (a) Sn 3d, (b) Zr 3d, and (c) O 1 s and Sb 3d core level XPS of as-deposited and 5×10^{15} ions/cm^2 Sb^+ implanted SnO_2 colloidal thin films.

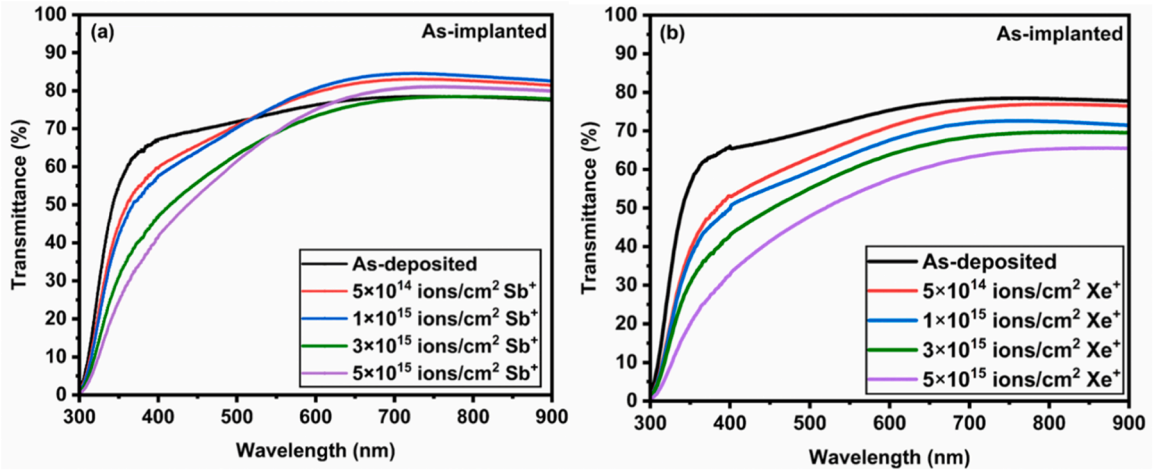

Fig. 4. UV-Vis spectra of SnO_2 colloidal films deposited on glass substrates: (a) implanted with Sb^+ and (b) implanted with Xe^+.

annealing at an elevated temperature of 300 °C revealed distinctive behaviors between the samples implanted with antimony and those implanted with xenon. For the antimony-implanted films, the higher temperature further reduced resistivity, with the highest fluence 5×10^{15} ions/cm^2 sample reaching (149.3 ± 4.3) μΩ cm, while for the same fluence, the Xe resistivity doubles to a value of (313.0 ± 9.1) μΩ cm.

Fig. 6 illustrates the carrier concentration (n_H) on (a) Sb-implanted and (b) Xe-implanted colloidal SnO_2 films, and subjected to annealing treatments at 200 °C and 300 °C. In the as-implanted state, after Sb implantation, the carrier concentration exhibits a steady decrease from $(7.8 \pm 0.2) \times 10^{20}$ cm^{-3} to $(5.7 \pm 0.2) \times 10^{20}$ cm^{-3} as the implantation fluence increases. Following annealing at 200 °C in air an increase in carrier concentration was observed, with values ranging from $(7.5 \pm 0.2) \times 10^{20}$ cm^{-3} with fluence of 5×10^{14} ions/cm^2 to $(9.1 \pm 0.3) \times 10^{20}$ cm^{-3} for the highest fluence of 5×10^{15} ions/cm^2. A comparable trend is observed for the Xe implantation series. However, at a higher annealing temperature of 300 °C the carrier concentrations of Sb-implanted and Xe-implanted samples differ. For the Sb-implanted films, an additional increase in carrier concentration was observed, reaching $(9.9 \pm 0.3) \times 10^{20}$ cm^{-3} for the highest fluence of 5×10^{15} ions/cm^2. In contrast, Xe-implanted films show a significant reduction of the carrier concentration to a value of $(4.9 \pm 0.2) \times 10^{20}$ cm^{-3} for the highest fluence of 5×10^{15} ions/cm^2, even below the concentration of $(6.3 \pm 0.2) \times 10^{20}$ cm^{-3} obtained prior to annealing.

The electrical properties highlight that the change in the resistivity is predominately determined by the change of the charge carrier concentration, since the charge carrier mobility is almost constant for all samples (Figure S5). We attribute the reduction of the number of charge carriers after ion implantation to radiation damage which causes the formation of compensating acceptor states, such as oxygen interstitials (O_i) and tin vacancies (V_{Sn}). These defects trap electrons, leading to a reduction in free carrier concentration and an increase in the electrical resistivity of the films [20,40].

Even a moderate thermal treatment (>200 ℃) is sufficient to remove these defects, leading to an overall enhancement of carrier concentration in the colloidal film. In addition, the treatment of the antimony-implanted colloidal films leads to an activation of the electron donor

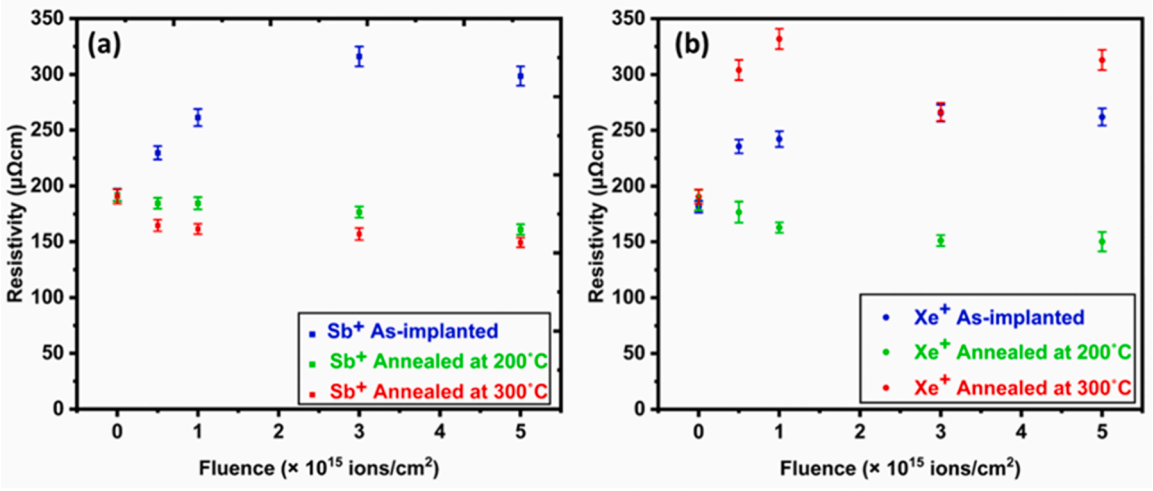

Fig. 5. Room temperature electrical resistivity (ρ) of SnO_2 colloidal films as a function of fluence for: (a) Sb^+ implantation (closed squares) and (b) Xe^+ implantation (closed circles), measured in as-implanted films and after annealing at 200 °C and 300 °C.

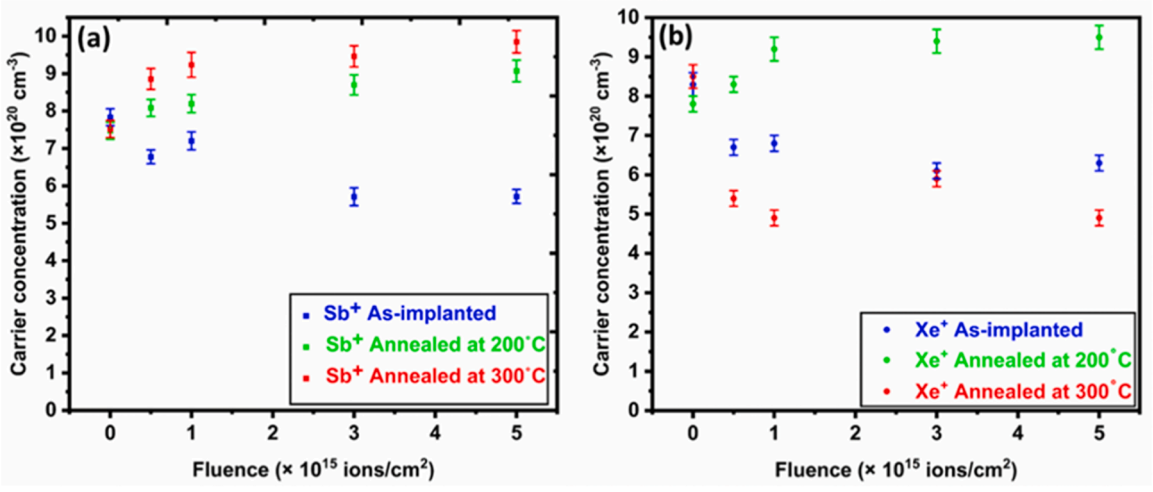

Fig. 6. Hall carrier concentration (n_H) of SnO_2 colloidal films as a function of fluence for As-implanted, annealed at 200 °C and annealed at 300 °C. The data is represented as follows: (a) closed squares represent the Sb^+ implantation and (b) closed circles represent the Xe^+.

attributed to the ratio Sb^{3+} and Sb^{5+} ions present in the lattice [24]. The presence of Sb^{5+} contributes additional free electrons to the conduction band, thereby enhancing conductivity and increasing the charge carrier concentration [12,23,24]. Sb^{5+} ions substitute for Sn^{4+} in the lattice, creating shallow donor levels within the material [17]. Xe implantation is known to introduce shallow defect levels on the surface of wide band gap semiconductors, caused predominately by nuclear stopping [19,41]. The presented results are thus consistent with the formation of shallow defects due to ion implantation. In addition, the colloidal form of the deposited film enhances the effective surface area. Physical vapor deposited Sb-doped SnO_2 films have shown a dramatic reduction of resistivity in the temperature range between 200℃ and 300℃, attributed to the chemical activation of defects by Sb in reaction with water vapor [20]. That transition range does contribute to the observed differences between Sb and Xe implantation. For Sb implantation, the beneficial shallow defects are stable at 300℃ and additional donor sites are created due to the substitutional incorporation of Sb into the SnO_2 lattice. In contrast, after Xe implantation, the weaker interaction with SnO_2 leads to the annihilation of the carrier concentration enhancing defects.

We have demonstrated that ion implantation effectively enhances the electrical conductivity and thermal stability of colloidal SnO_2 thin films, making them more efficient as charge transporting layers. Specifically, the resistivity of the film is reduced from (187.6 ± 8.1) μΩ cm to (150.2 ± 8.7) μΩ cm for xenon and annealed at 200 °C and to (160.8 ± 4.7) μΩ cm for antimony. We have demonstrated that at a post-implantation annealing temperature up to 200℃, the difference between

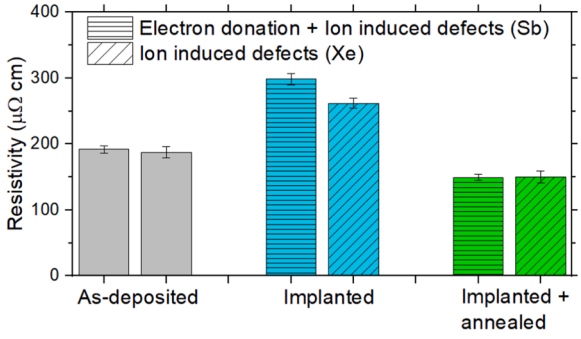

Fig. 7. Comparison of Sb and Xe samples after as-deposited, after ion implantation to a fluence of 5×10^{15} at.cm^{-2} (implanted) and the ion implantation (5×10^{15} at.cm^{-2}) followed by thermal annealing at 200 ℃ (implanted + annealed).

the chemical contribution of electron-donating Sb^+, in comparison to non-electron donating Xe^+ is irrelevant for the materials resistivity (Fig. 7). In contrast a change in fluence causes a consistent variation, highlighting the importance of the oxygen vacancy formation.

This implies that the resistivity, charge carrier concentration and mobility are solely determined by the introduced defects into SnO_2 and no significant contribution from electron donation of Sb occurs.

Only samples annealed at 300 °C after ion implantation show a deviation. For antimony the resistivity reduces even further to (149.3 ± 4.3) μΩ cm, while the resistivity of Xe implantation doubles to (313.0 ± 9.1) μΩ cm. This effect is attributed to the higher stability of the introduced defects in the presence of Sb. In all cases, implantation reduces transparency in the wavelength range of 400–500 nm which is more pronounced for xenon implantation. Hence, antimony implantation is only the preferred choice if a subsequent high temperature process or exceptional transmittance is required.

4. Conclusion

We designed an experiment to reveal if the electrical performance of SnO_2 nanoparticles films is dominated by electron donation or vacancy formation. Ion implantation of elements with similar mass of Sb and Xe with the same acceleration energy to the same fluence provides an identical formation of vacancies in the deposited SnO_2 film. The comparison of the resistivity reveals that these are similar up to an annealing temperature of 200℃. Hence, the effect of Sb electron donation is negligible in these films. Our results imply that strategies to improve the electrical properties of ETLs in PSC should focus on optimising vacancy formation.

CRediT authorship contribution statement

Kennedy John: Writing – review & editing, Supervision, Funding acquisition. **Holger Fiedler:** Writing – review & editing, Visualization, Supervision, Funding acquisition. **Zhan Chen:** Writing – review & editing, Supervision. **Maziar Ramezani:** Writing – review & editing, Supervision. **Abubakar Sadiq Yusuf:** Writing – review & editing, Writing – original draft, Resources, Methodology, Conceptualization. **Martin Markwitz:** Writing – review & editing, Visualization.

Declaration of Competing Interest

The authors declare that they have no known competing financial interests or personal relationships that could have appeared to influence the work reported in this paper.

Acknowledgements

Abubakar Sadiq Yusuf would like to thank the Tertiary Education Trust Fund (Tetfund) for funding TETF/ES/UNIV/NIGER STATE/TSAS/2020. This project was partly funded by the Royal Society of New Zealand under Marsden contract MFP-GNS2202 and by the New Zealand Ministry for Business, Innovation and Employment through the Materials for Low Carbon Future Program (C05X1702). The authors would like to acknowledge Chris Purcell at the National Isotope Centre of GNS Science in New Zealand for the RBS measurements, and the surface analysis laboratory at UNSW in Australia for the XPS measurements.

Appendix A. Supporting information

Supplementary data associated with this article can be found in the online version at doi:10.1016/j.nxmate.2026.102284.

Data availability

Data can be made available upon reasonable request.

References

[1] S.A. Abubaker, M.Z. Pakhuruddin, An Overview of Electron Transport Layer Materials and Structures for Efficient Organic Photovoltaic Cells, Energy Technol. 12 (9) (2024) 2400285, https://doi.org/10.1002/ente.202400285.
[2] Q. Dong, M. Wang, Q. Zhang, F. Chen, S. Zhang, J. Bian, T. Ma, L. Wang, Y. Shi, *Discontinuous SnO_2 derived blended-interfacial-layer in mesoscopic perovskite solar cells: Minimizing electron transfer resistance and improving stability.* Nano Energy 38 (2017) 358–367, https://doi.org/10.1016/j.nanoen.2017.05.058.
[3] C. Altinkaya, E. Aydin, E. Ugur, F.H. Isikgor, A.S. Subbiah, M. De Bastiani, J. Liu, A. Babayigit, T.G. Allen, F. Laquai, A. Yildiz, S. De Wolf, Tin Oxide Electron-Selective Layers for Efficient, Stable, and Scalable Perovskite Solar Cells, Adv. Mater. 33 (15) (2021) 2005504, https://doi.org/10.1002/adma.202005504.
[4] K. Aguir, S. Bernardini, B. Lawson, T. Fiorido, Trends in metal oxide thin films: Synthesis and applications of tin oxide, in: M.O. Orlandi (Ed.), Tin Oxide Materials, Elsevier, 2020, pp. 219–246.
[5] D. Filatova, M. Rumyantseva, Additives in Nanocrystalline Tin Dioxide: Recent Progress in the Characterization of Materials for Gas Sensor Applications, Materials 16 (2023), https://doi.org/10.3390/ma16206733.
[6] G.K. Dalapati, H. Sharma, A. Guchhait, N. Chakrabarty, P. Bamola, Q. Liu, G. Saianand, A.M. Sai Krishna, S. Mukhopadhyay, A. Dey, T.K.S. Wong, S. Zhuk, S. Ghosh, S. Chakrabortty, C. Mahata, S. Biring, A. Kumar, C.S. Ribeiro, S. Ramakrishna, A.K. Chakraborty, S. Krishnamurthy, P. Sonar, M. Sharma, Tin oxide for optoelectronic, photovoltaic and energy storage devices: a review, J. Mater. Chem. A 9 (31) (2021) 16621–16684, https://doi.org/10.1039/D1TA01291F.
[7] Ç. Kılıç, A. Zunger, *Origins of Coexistence of Conductivity and Transparency in SnO_2*, Phys. Rev. Lett. 88 (9) (2002) 095501, https://doi.org/10.1103/PhysRevLett.88.095501.
[8] M. Worsdale, A. Rabis, E. Fabbri, T.J. Schmidt, D. Kramer, *Conductivity Limits of Extrinsically Doped SnO_2 Supports.* ECS Trans. 69 (17) (2015) 1167, https://doi.org/10.1149/06917.1167ecst.
[9] R.F. Martinez-Gazoni, M.W. Allen, R.J. Reeves, *Conductivity and transparency limits of Sb-doped SnO_2 grown by molecular beam epitaxy.* Phys. Rev. B 98 (15) (2018) 155308 https://doi.org/10.1103/PhysRevB.98.155308.
[10] W. Yang, S. Yu, Y. Zhang, W. Zhang, *Properties of Sb-doped SnO_2 transparent conductive thin films deposited by radio-frequency magnetron sputtering.* Thin Solid Films 542 (2013) 285–288, https://doi.org/10.1016/j.tsf.2013.06.077.
[11] C. Luan, Z. Zhu, W. Mi, J. Ma, *Effect of Sb doping on structural, electrical and optical properties of epitaxial SnO_2 films grown on r-cut sapphire.* J. Alloy. Compd. 586 (2014) 426–430, https://doi.org/10.1016/j.jallcom.2013.10.087.
[12] M. Esro, S. Georgakopoulos, H. Lu, G. Vourlias, A. Krier, W.I. Milne, W.P. Gillin, G. Adamopoulos, *Solution processed SnO_2:Sb transparent conductive oxide as an alternative to indium tin oxide for applications in organic light emitting diodes.* J. Mater. Chem. C. 4 (16) (2016) 3563–3570, https://doi.org/10.1039/C5TC04117A.
[13] L. Liu, S. Ma, H. Wu, B. Zhu, H. Yang, J. Tang, X. Zhao, *Effect of the annealing process on electrical and optical properties of SnO_2/Ag/SnO_2 nanometric multilayer film.* Mater. Lett. 149 (2015) 43–46, https://doi.org/10.1016/j.matlet.2015.02.093.
[14] J.-L. Huang, Y. Pan, J.Y. Chang, B.-S. Yau, Annealing effects on properties of antimony tin oxide thin films deposited by RF reactive magnetron sputtering, Surf. Coat. Technol. 184 (2) (2004) 188–193, https://doi.org/10.1016/j.surfcoat.2003.11.004.
[15] P. Ágoston, K. Albe, R.M. Nieminen, M.J. Puska, *Intrinsic n-Type Behavior in Transparent Conducting Oxides: A Comparative Hybrid-Functional Study of In_2O_3, SnO_2, and ZnO.* Phys. Rev. Lett. 103 (24) (2009) 245501 https://doi.org/10.1103/PhysRevLett.103.245501.
[16] C.A. Hoel, T.O. Mason, J.-F. Gaillard, K.R. Poeppelmeier, *Transparent Conducting Oxides in the ZnO-In_2O_3-SnO_2 System.* Chem. Mater. 22 (12) (2010) 3569–3579, https://doi.org/10.1021/cm1004592.
[17] M. Sun, J. Liu, B. Dong, *Effects of Sb doping on the structure and properties of SnO_2 films.* Curr. Appl. Phys. 20 (3) (2020) 462–469, https://doi.org/10.1016/j.cap.2020.01.009.
[18] Y. Bai, Y. Fang, Y. Deng, Q. Wang, J. Zhao, X. Zheng, Y. Zhang, J. Huang, *Low Temperature Solution-Processed Sb:SnO_2 Nanocrystals for Efficient Planar Perovskite Solar Cells.* ChemSusChem 9 (18) (2016) 2686–2691, https://doi.org/10.1002/cssc.201600944.
[19] M. Markwitz, P.P. Murmu, T. Mori, J.V. Kennedy, B.J. Ruck, Defect engineering-induced Seebeck coefficient and carrier concentration decoupling in CuI by noble gas ion implantation, Appl. Phys. Lett. 125 (21) (2024) 213901, https://doi.org/10.1063/5.0233754.
[20] C.S. Rastomjee, R.S. Dale, R.J. Schaffer, F.H. Jones, R.G. Egdell, G.C. Georgiadis, M.J. Lee, T.J. Tate, L.L. Cao, *An investigation of doping of SnO_2 by ion implantation and application of ion-implanted films as gas sensors.* Thin Solid Films 279 (1) (1996) 98–105, https://doi.org/10.1016/0040-6090(95)08156-9.
[21] A.S. Yusuf, M. Markwitz, Z. Chen, M. Ramezani, J.V. Kennedy, H. Fiedler, *Optimizing the resistivity of colloidal SnO_2 thin films by ion implantation and annealing.* Surf. Interfaces (2024) 105325 https://doi.org/10.1016/j.surfin.2024.105325.
[22] M. Al Hashem, S. Akbar, P. Morris, Role of Oxygen Vacancies in Nanostructured Metal-Oxide Gas Sensors: A Review, Sens. Actuators B Chem. 301 (2019) 126845, https://doi.org/10.1016/j.snb.2019.126845.
[23] J. Guo, R. Zhang, C. Li, C. Gong, J. Zhang, J. Zhang, Sb-doped tin oxide nanonets for improved conductivity in transparent conductive coatings, Mater. Chem. Phys. 320 (2024), https://doi.org/10.1016/j.matchemphys.2024.129476.

[24] S. Gupta, B.C. Yadav, P.K. Dwivedi, B. Das, *Microstructural, optical and electrical investigations of Sb-SnO_2 thin films deposited by spray pyrolysis.* Mater. Res. Bull. 48 (9) (2013) 3315–3322, https://doi.org/10.1016/j.materresbull.2013.05.001.
[25] J.M. Colwell, E. Wentrup-Byrne, J.M. Bell, L.S. Wielunski, A study of the chemical and physical effects of ion implantation of micro-porous and nonporous PTFE, Surf. Coat. Technol. 168 (2-3) (2003) 216–222, https://doi.org/10.1016/S0257-8972(03)00204-4.
[26] H. Fiedler, P. Gupta, J. Kennedy, A. Markwitz, 28)Si(+) ion beams from Penning ion source based implanter systems for near-surface isotopic purification of silicon, Rev. Sci. Instrum. 89 (12) (2018) 123305, https://doi.org/10.1063/1.5048949.
[27] J.P. Biersack, S. Berg, C. Nender, T-DYN Monte Carlo simulations applied to ion assisted thin film processes, Nucl. Instrum. Methods Phys. Res. Sect. B Beam Interact. Mater. At. 59-60 (1991) 21–27, https://doi.org/10.1016/0168-583X(91)95167-C.
[28] N. Fairley, V. Fernandez, M. Richard-Plouet, C. Guillot-Deudon, J. Walton, E. Smith, D. Flahaut, M. Greiner, M. Biesinger, S. Tougaard, D. Morgan, J. Baltrusaitis, Systematic and collaborative approach to problem solving using X-ray photoelectron spectroscopy, Appl. Surf. Sci. Adv. 5 (2021) 100112, https://doi.org/10.1016/j.apsadv.2021.100112.
[29] I.M. Costa, Y.N. Colmenares, P.S. Pizani, E.R. Leite, A.J. Chiquito, *Sb doping of VLS synthesized SnO_2 nanowires probed by Raman and XPS spectroscopy.* Chem. Phys. Lett. 695 (2018) 125–130, https://doi.org/10.1016/j.cplett.2018.02.014.
[30] J.V. Kennedy, W.J. Trompetter, P.P. Murmu, J. Leveneur, P. Gupta, H. Fiedler, F. Fang, J. Futter, C. Purcell, Evolution of Rutherford's ion beam science to applied research activities at GNS Science, J. R. Soc. N. Z. 51 (3-4) (2021) 574–591, https://doi.org/10.1080/03036758.2021.1897021.
[31] M. Batzill, U. Diebold, The surface and materials science of tin oxide, Prog. Surf. Sci. 79 (2) (2005) 47–154, https://doi.org/10.1016/j.progsurf.2005.09.002.
[32] M. Mayer, SIMNRA Use 's. Guide (1997).
[33] E. Payen, L. Gengembre, F. Mauge, J.C. Duchet, J.C. Lavalley, Surface properties of zirconia catalyst carriers: interaction with oxomolybdates species, Catal. Today 10 (4) (1991) 521–539, https://doi.org/10.1016/0920-5861(91)80037-A.
[34] J. Heo, A.S. Hock, R.G. Gordon, Low Temperature Atomic Layer Deposition of Tin Oxide, Chem. Mater. 22 (17) (2010) 4964–4973, https://doi.org/10.1021/cm1011108.
[35] A.R. Babar, S.S. Shinde, A.V. Moholkar, C.H. Bhosale, J.H. Kim, K.Y. Rajpure, Structural and optoelectronic properties of antimony incorporated tin oxide thin films, J. Alloy. Compd. 505 (2) (2010) 416–422, https://doi.org/10.1016/j.jallcom.2010.06.091.
[36] B.B. Harbison, B.H. Rabin, S.R. Shatynski, Optical Properties of Ion Implanted Indium Tin Oxide Glasses, in: R. Kossowsky, S.C. Singhal (Eds.), Surface Engineering: Surface Modification of Materials, Springer Netherlands, Dordrecht, 1984, pp. 111–124.
[37] K.H. Kim, S.W. Lee, D.W. Shin, C.G. Park, Effect of Antimony Addition on Electrical and Optical Properties of Tin Oxide Film, J. Am. Ceram. Soc. 77 (4) (1994) 915–921, https://doi.org/10.1111/j.1151-2916.1994.tb07247.x.
[38] I. Saadeddin, H.S. Hilal, B. Pecquenard, J. Marcus, A. Mansouri, C. Labrugere, M. A. Subramanian, G. Campet, *Simultaneous doping of Zn and Sb in SnO_2 ceramics: Enhancement of electrical conductivity.* Solid State Sci. 8 (1) (2006) 7–13, https://doi.org/10.1016/j.solidstatesciences.2005.09.002.
[39] M. Kanamori, K. Suzuki, Y.O. Yutaka Ohya, Y.T. Yasutaka Takahashi, *Analysis of the Change in the Carrier Concentration of SnO_2 Thin Film Gas Sensor.* Jpn. J. Appl. Phys. 33 (12R) (1994) 6680, https://doi.org/10.1143/JJAP.33.6680.
[40] Z. Tao, H. Junda, L. Hong, Modification of tin dioxide thin films by ion implantation, Appl. Surf. Sci. 161 (3) (2000) 459–464, https://doi.org/10.1016/S0169-4332(00)00359-7.
[41] H. Fiedler, J. Hardy, J.E. Halpert, N.J.L.K. Davis, J. Kennedy, *Shallow defects and optical properties of $CsPbBr_3$ thin films through noble gas ion beam defect engineering.* Nanotechnology 36 (6) (2025) 065202 https://doi.org/10.1088/1361-6528/ad91bd.